However, the large asymmetry of the band structure in this compound (*17*) can also lead to a photodoping effect: The electrons and holes scatter and lose energy at different rates, leading to a transient imbalance of their respective populations, n_e and n_h, within less than 5 ps.

A photodoped hole in this system annihilates with the localized 13th electron; this process removes the charge at the center of the polaron, leaving a void in the place of the polaronic distortion. Because some of the 13th electrons have been annihilated by holes, not all ions in these regions are charge-compensated, and they have an excess charge. Yet these regions cannot conduct because the remaining 12 electrons are in filled states within the gap formed by the long-range CDW (Fig. 3C). The excess charge will be screened by the electrons, which are now transferred to the delocalized bands. At a sufficiently high concentration n_v, these voids are expected to aggregate by diffusion into domain walls. The overall state becomes conducting via the band states released by the annihilated polarons, which, if ordered, would form a new ordered structure of polaron clusters separated by domain walls, as indicated schematically in Fig. 3A. We can also imagine that photoexcited electrons could squeeze into the structure in between the polarons, creating interstitials with a concentration n_i (*11*). Together with voids with a concentration n_v, the total "intrinsic defect" concentration $n_d = n_v - n_i$ may have either sign. Overall charge conservation $n_h + n_v = n_e + n_i$ gives the imbalance of the current carriers, $n_d = n_e - n_h$.

The value of n_d is related to deviations $\delta q/\pi \approx -n_d$ of the CDW wave vector q with respect to the C state. Conventionally, photodoping is a transient effect, so once *e-h* symmetry is recovered, the voids and domain walls disappear and the C state is restored. However, if the voids can be stabilized by collectively ordering into a long-range ordered state, the final state is different from the original one. The free energy $F_d(n_d)$ appropriate for the formation of the charge-ordered state outlined above (*19*) needs to include the effect of repulsion between the domain walls and between their crossings (*19*, *25*, *26*), and should reproduce the first-order nature of the transition (*19*, *26*). Values of $F_d(n_d)$ based on these considerations and existing models (*19*, *26*) are plotted in Fig. 3B. The time dependencies of concentrations $n_e(t)$ and $n_h(t)$ are calculated in (*14*).

The model (*14*) is consistent with the main experimental observations, namely the appearance of a switching threshold for the W pulse fluence, its critical pulse-length dependence, the threshold temperature for the E cycle, the high conductance, and the remarkable stability of the H state. The switching is caused by relatively weak and short pulses, which—considering the large change in resistance and optical reflectivity—has potential for device applications. The effect will also stimulate the search for new generations of room-temperature nonvolatile memory elements in electronically ordered materials. As a memory element switchable by 35-fs pulses, our device is already comparable to the current speed record of 40 fs in magnetic materials (*28*).

References and Notes

1. S. Koshihara, Y. Tokura, T. Mitani, G. Saito, T. Koda, *Phys. Rev. B* **42**, 6853–6856 (1990).
2. K. Nasu, *Photoinduced Phase Transitions* (World Scientific, Singapore, 2004).
3. H. Okamoto *et al.*, *Phys. Rev. B* **70**, 165202 (2004).
4. A. Cavalleri *et al.*, *Phys. Rev. Lett.* **87**, 237401 (2001).
5. S. Tomimoto, S. Miyasaka, T. Ogasawara, H. Okamoto, Y. Tokura, *Phys. Rev. B* **68**, 035106 (2003).
6. N. Takubo *et al.*, *Phys. Rev. Lett.* **95**, 017404 (2005).
7. K. Nasu, H. Ping, H. Mizouchi, *J. Phys. Condens. Matter* **13**, R693–R721 (2001).
8. G. Yu, C. H. Lee, A. J. Heeger, N. Herron, E. M. McCarron, *Phys. Rev. Lett.* **67**, 2581–2584 (1991).
9. D. Fausti *et al.*, *Science* **331**, 189–191 (2011).
10. A. Zakery, S. R. Elliott, *Optical Nonlinearities in Chalcogenide Glasses and Their Applications* (Springer, New York, 2007).
11. R. Thomson, B. Burk, A. Zettl, J. Clarke, *Phys. Rev. B* **49**, 16899–16916 (1994).
12. B. Sipos *et al.*, *Nat. Mater.* **7**, 960–965 (2008).
13. L. J. Li *et al.*, *Eur. Phys. Lett.* **97**, 67005 (2012).
14. See supplementary materials on *Science* Online.
15. T. Ishiguro, H. Sato, *Phys. Rev. B* **44**, 2046–2060 (1991).
16. J. Demsar, L. Forro, H. Berger, D. Mihailovic, *Phys. Rev. B* **66**, 041101 (2002).
17. K. Rossnagel, N. V. Smith, *Phys. Rev. B* **73**, 073106 (2006).
18. E. Tosatti, P. Fazekas, *J. Phys. Colloq.* **37**, C4-165–C4-168 (1976).
19. K. Nakanishi, H. Shiba, *J. Phys. Soc. Jpn.* **43**, 1839–1847 (1977).
20. J. C. Petersen *et al.*, *Phys. Rev. Lett.* **107**, 177402 (2011).
21. S. Hellmann *et al.*, *Phys. Rev. Lett.* **105**, 187401 (2010).
22. L. Perfetti *et al.*, *New J. Phys.* **10**, 053019 (2008).
23. M. Eichberger *et al.*, *Nature* **468**, 799–802 (2010).
24. F. Clerc *et al.*, *J. Phys. Condens. Matter* **19**, 355002 (2007).
25. W. McMillan, *Phys. Rev. B* **14**, 1496–1502 (1976).
26. P. Bak, *Rep. Prog. Phys.* **45**, 587 (1982).
27. N. Dean *et al.*, *Phys. Rev. Lett.* **106**, 016401 (2011).
28. A. Kirilyuk, A. V. Kimel, T. Rasing, *Rev. Mod. Phys.* **82**, 2731–2784 (2010).

Acknowledgments: Supported by the Slovenian Research Agency, European restructuring funds (CENN Nanocenter), and European Research Council advanced grant TRAJECTORY. A European patent application PCT/SI2013/000056 has been submitted. We thank L. Forro, V. V. Kabanov, N. Kirova, P. Monceau, E. Tossatti, and E. Tutis for valuable discussions.

Supplementary Materials

www.sciencemag.org/content/344/6180/177/suppl/DC1
Materials and Methods
Supplementary Text
Figs. S1 to S10
Table S1
References (*29*–*55*)

6 June 2013; accepted 13 March 2014
10.1126/science.1241591

Entangled States of More Than 40 Atoms in an Optical Fiber Cavity

Florian Haas, Jürgen Volz,* Roger Gehr, Jakob Reichel,† Jérôme Estève†

Multiparticle entanglement enables quantum simulations, quantum computing, and quantum-enhanced metrology. Yet, there are few methods to produce and measure such entanglement while maintaining single-qubit resolution as the number of qubits is scaled up. Using atom chips and fiber-optical cavities, we have developed a method based on nondestructive collective measurement and conditional evolution to create symmetric entangled states and perform their tomography. We demonstrate creation and analysis of entangled states with mean atom numbers up to 41 and experimentally prove multiparticle entanglement. Our method is independent of atom number and should allow generalization to other entangled states and other physical implementations, including circuit quantum electrodynamics.

For entanglement-enabled technologies as well as from a fundamental point of view, an important goal is to scale up the number of entangled particles in many-qubit systems. In a bottom-up approach, individual addressing and universal quantum gates allow full control on the quantum state, and, in principle, any entangled state can be produced. However, because the number of gate operations scales up with particle number, experiments based on this method (such as ion traps) are currently limited to less than 20 entangled qubits (*1*).

Many important entangled states can be produced in a "top-down" approach with collective interactions or quantum nondemolition (QND) measurements, the complexity of which does not increase with particle number. In atomic ensembles, spin-squeezed (*2*, *3*) and twin Fock states (*4*) have been produced by collisional interactions; collective QND measurement (*5*–*8*) and cavity-mediated interactions (*9*) have been used to produce spin squeezing and have been proposed for Schrödinger cats (*10*) and Dicke states, including twin Fock states (*11*). However, state-of-the-art QND measurements in ensembles are still far from the single-particle resolution that would be required, for example, to reach the Heisenberg limit of quantum metrology (*12*). Moreover, the full quantum state of a system cannot be experimentally determined

Laboratoire Kastler Brossel, École Normale Supérieure, Université Pierre et Marie Curie–Paris 6, CNRS, 24 Rue Lhomond, 75005 Paris, France.

*Present address: Vienna Center for Quantum Science and Technology, Atominstitut, Vienna University of Technology, 1020 Vienna, Austria.

†Corresponding author. E-mail: esteve@lkb.ens.fr (J.E.); jakob.reichel@ens.fr (J.R.)

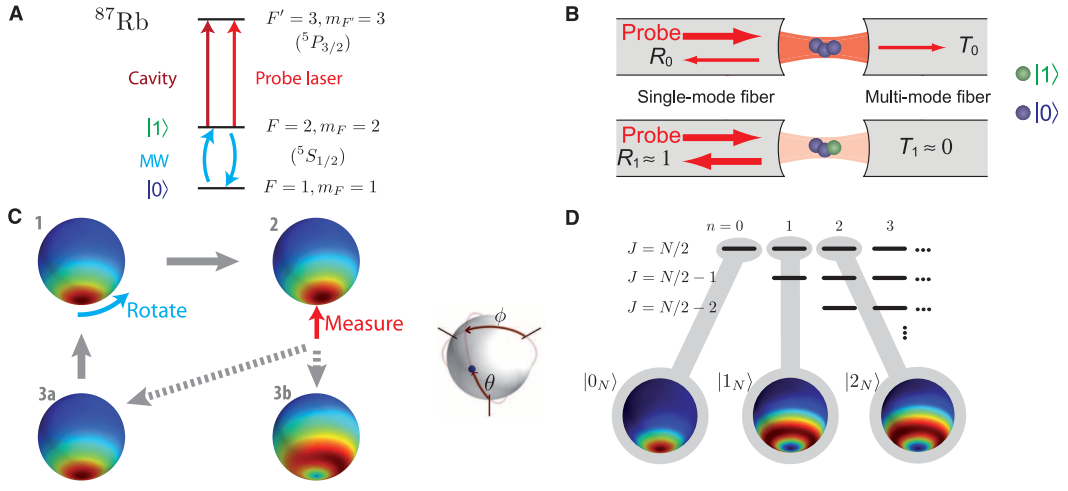

Fig. 1. Cavity-assisted generation of entanglement. (**A**) Relevant level scheme of ^{87}Rb. A resonant 6.8 GHz microwave allows applying arbitrary rotations to the atomic qubit. The cavity and probe laser are resonant with the transition $|1\rangle \rightarrow |F' = 3, m_{F'} = 3\rangle$, where F' and $m_{F'}$ denote the hyperfine and magnetic sublevels of the excited state, respectively. (*21*). MW, microwave pulse. (**B**) Principle of the collective QND measurement based on the normal-mode splitting. *R*, reflection; *T*, transmission. (**C**) Preparation sequence of the W state. The asymmetry in 3b originates from the nonzero contribution of higher-order Dicke states, which is due to the finite value of *p*. (**D**) The spin states with norm *J* and *z* component $-J + n$, where $2J \geq n \geq 0$, form a basis for the total atomic pseudospin (with this notation, *n* is the number of atoms in $|1\rangle$). In the symmetric subspace ($J = N/2$), the atomic state is fully characterized by its Husimi *Q* distribution, measured in our experiment. Shown are calculated distributions for the $|0_N\rangle$, $|1_N\rangle$, and $|2_N\rangle$ Dicke states.

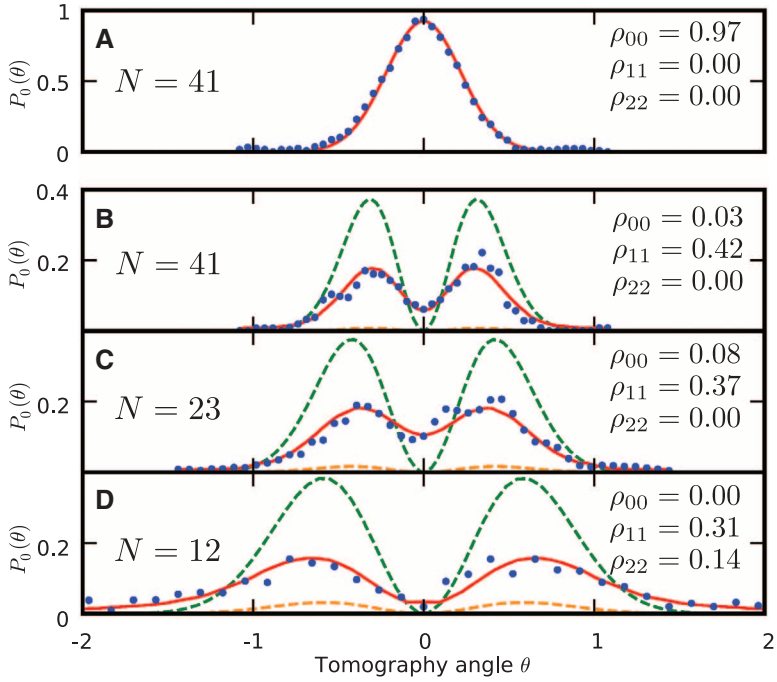

Fig. 2. Tomography of coherent and W states. (**A**) Tomography of a coherent state $|0_N\rangle$ (the initial state before the W state preparation). From a fit (red line), we obtain the number of atoms, $N = 41$. (**B** to **D**) Tomography of W states with 41, 23, and 12 atoms, respectively. Each point corresponds to ~50 measurements. For each atom number, the red curve results from a maximum likelihood state reconstruction taking into account all known imperfections of the tomography technique (*21*). For comparison, the dashed green lines show the theoretical $P_0(\theta)$ for an ideal W state, and the dashed orange lines indicate that of a statistical mixture in which one known atom among *N* is in $|1\rangle$. For each *N*, the populations of the $|0_N\rangle$ state and the first and second Dicke states $|1_N\rangle$ and $|2_N\rangle$ are indicated, as deduced from the state reconstruction.

nor efficiently analyzed beyond 10 to 20 qubits, in general (*13*), so that new methods that specifically identify and characterize relevant forms of entanglement in large systems are required.

Here, we use a cavity-based measurement that distinguishes one particular many-particle quantum state from the orthogonal subspace of all other states. This allows us to prepare many-body entangled states projectively and to directly measure their quasiprobability distribution with high resolution. Consider an ensemble of *N* atoms, all strongly coupled to a single mode of a high-finesse cavity (*14*–*18*) (Fig. 1, A and B). The cavity and probe beam are tuned for detecting the hyperfine state, $|0\rangle$ or $|1\rangle$ (*19*). Transmission through the cavity is observed only when all *N* atoms are in $|0_N\rangle \equiv |0\ldots0\rangle$. A single atom in $|1\rangle$ makes the cavity fully reflecting (*20*), and no further substantial changes occur when more than one atom is in $|1\rangle$. Due to the very strong coupling of the atom-resonator system (*21*), this is true for all atomic positions, so that the atoms are indistinguishable when probed by the cavity mode. Furthermore, we set the probe power such that the total probability for a spontaneous emission event is much smaller than one (*19*), limiting the amount of atom-distinguishing information that leaks into the environment. Thus, to good approximation, measuring the cavity transmission is a projective measurement with two eigenvalues: high transmission corresponding to $|0_N\rangle$ and low transmission to the orthogonal subspace containing all other states, where at least one atom is in $|1\rangle$. This measurement enables the generation of multiparticle entanglement as follows: Atoms are prepared in a premeasurement state $|\Psi\rangle$, then are measured as described. Low transmission signals preparation of $|0_N\rangle$ (meaning that the cycle must be repeated), whereas high transmission prepares the system in $|\xi\rangle \equiv c(\mathbb{1} - |0_N\rangle\langle 0_N|)|\Psi\rangle$, where *c* is a normalization factor. For a suitable choice of $|\Psi\rangle$, $|\xi\rangle$ can have interesting nonclassical properties. Here, we prepare a $|\xi\rangle$ that is a good approximation of

$$|1_N\rangle \equiv \frac{1}{\sqrt{N}}(|10\ldots0\rangle + |010\ldots0\rangle + \ldots + |00\ldots1\rangle) \quad (1)$$

known as the W state or the first Dicke state. It represents a fundamental class of entangled states (*22*), which are robust against particle loss and enable some meteorological gain over nonentangled states (*23*).

To obtain the W state, we start from $|0_N\rangle$ and apply a weak coherent microwave pulse on the qubit transition. If the excitation probability *p* is small, this prepares $|\Psi\rangle = \sqrt{1-p}|0_N\rangle + \sqrt{p}|1_N\rangle$. Measuring $|\Psi\rangle$ as described either projects back onto $|0_N\rangle$ or prepares $|1_N\rangle$. Low transmission heralds successful preparation, and the state is then available for further experiments. Figure 1C shows the expected evolution during the sequence.

Note that the system is always in a known, pure state, as in a quantum feedback scheme, and in contrast to single-photon heralded schemes (*24*, *25*).

To fully characterize the produced state, we have developed a tomography technique that measures the Husimi Q distribution of the total spin (*26*). In the ideal sequence (Fig. 1C), the state evolves inside the symmetric subspace, which contains the states with maximum pseudo-spin $J = N/2$ (Fig. 1D). In this subspace, which is spanned by the Dicke states and can be represented on a generalized Bloch sphere, the Q function is defined as $Q(\theta,\phi) = (N+1)/(4\pi)\, P_0(\theta,\phi)$ (*26*), where $P_0(\theta,\phi) = \langle 0_N | R^{\dagger}_{\theta,\phi} \rho R_{\theta,\phi} | 0_N \rangle$ is the probability that all atoms are in $|0_N\rangle$ after a rotation $R_{\theta,\phi}$ of the state with density matrix ρ. This expression shows that a direct measurement of Q is obtained by combining a rotation $R_{\theta,\phi}$ (performed with a microwave pulse here) with the measurement described above. Indeed, the probability to obtain high transmission for a given state measures its overlap with $|0_N\rangle$ (*21*, *27*). This method strongly differs from marginal distribution measurements (*3*, *28*) and is similar to one developed in quantum optics (*29*). Note that our binary individual measurement is sufficient to distinguish all symmetric states in the tomography when performed with a sufficient number of repetitions. For states outside the symmetric subspace ($J < N/2$), spin conservation under $R_{\theta,\phi}$ entails that they never transform into $|0_N\rangle$ and, thus, have a zero contribution to the measured P_0 for all (θ,ϕ) (Fig. 1D) (*21*). Therefore, the norm of Q of a given state yields its probability of lying in the symmetric subspace, whereas the shape of $Q(\theta,\phi)$ fully characterizes the symmetric part of the state.

In our experiment, a small atom number is prepared from an ultracold ensemble close to quantum degeneracy and trapped in a single antinode of a one-dimensional intracavity optical lattice, where each atom is strongly coupled to the resonant cavity mode (*15*, *21*). Figure 2A shows the tomography curve $P_0(\theta) \equiv P_0(\theta,\phi=0)$ for $|0_N\rangle$, the state before the preparation sequence. The measured curve is well approximated by the expected $\cos^{2N}(\theta/2)$, from which we deduce the mean number of atoms N that contribute to the state. Because of our atom number preparation (*21*), we expect the prepared atom number to follow a binomial distribution with SD σ = 4.2, 3.6, and 2.8 for N = 41, 23, and 12.

Applying the entanglement preparation method [see (*21*) for experimental details], the tomography results $P_0(\theta)$ of the prepared W states for N = 41, 23, 12 are shown in Fig. 2, B to D. The curves feature the characteristic central dip expected for the nonclassical W state. The nonzero value for $\theta = 0$ indicates some remnant population in $|0_N\rangle$, which is below 10% for all atom numbers. In addition, the curves have a high contrast, indicating a population in the symmetric subspace above 40% for all atom numbers. This clearly sets them apart from their classical counterparts, the statistical mixtures of all states with one localized excitation, $\{|100\ldots\rangle, |010\ldots\rangle, \ldots\}$ (orange curves in Fig. 2, B to D). For those states, the symmetric subspace population is only $1/N$, so that the maximum value of $P_0(\theta)$ is small.

Because of the rotational symmetry of the state, a fair estimate of the W state fidelity is obtained from the single polar cut $\phi = 0$ of the Q distribution. In fact, we expect that other cuts do not contain additional information because of a slow drift of the magnetic field during the long acquisition time of our data (several days), which randomizes the phases between the different Dicke states. This can be seen in the symmetry of the tomography data shown in Fig. 2 [$P_0(-\theta) \approx P_0(\theta)$]. We also measured $P_0(\theta, \phi = \pi/2)$ and verified that it is very similar to $P_0(\theta,0)$. To partially reconstruct the density matrix ρ in the Dicke basis, we make the simplifying assumption that ρ is purely diagonal and deduce the populations ρ_{ii} using a maximum likelihood algorithm. We have checked that this assumption does not overestimate the fidelity ρ_{11}, nor does it underestimate ρ_{00} for our data (*21*). The red solid lines in Fig. 2 show the tomography curves corresponding to the reconstructed density matrices displayed as insets, where we truncated the basis to the first three Dicke states (0 to 2 atoms in $|1\rangle$) (*21*). A fidelity ρ_{11} of 0.42, 0.37, and 0.31 was obtained for N = 41, 23, and 12. The 1σ error is below 0.1 in all cases (*21*).

One important limit to the fidelity is false-positive detection during preparation (atoms detected in $|1_N\rangle$ although they are in $|0_N\rangle$). Discarding runs with ambiguous measurement results reduces this error and increases fidelity, at the cost of reducing success probability. To decide whether the cavity is in the high- or low-transmission state, we analyze both the reflected and transmitted photon numbers, N_R and N_T, and compare to predefined thresholds. Figure 3A shows the count distribution of N_R (*21*). All data was acquired using $N_T = 0$, $N_R \geq 4$ as the criterion signaling successful preparation, leaving room for postselection using a higher threshold $N_{R,min}$. Figure 3B shows the fidelity as a function of $N_{R,min}$, confirming that this is an important contribution to the preparation error. The data shown in Fig. 2 correspond to values of $N_{R,min}$ [slightly different for each atom number (*21*)] such that the fraction of successful runs is ~10%.

Knowing how much entanglement is present in a many-particle state is difficult, even when the full density matrix is known. We now establish criteria for entanglement in the vicinity of the W state by solely comparing the two populations ρ_{00} and ρ_{11}. Bipartite entanglement being extremely difficult to prove with a W state (*30*), we rather look for multipartite entanglement and for the minimal number of entangled atoms. A state with density matrix ρ contains, at most, k entangled particles if ρ can be decomposed as a convex sum of density matrices $\rho_1 \otimes \ldots \otimes \rho_M$, where each ρ_i corresponds to a density matrix containing, at most, k atoms, and $M \leq N$ (*30*).

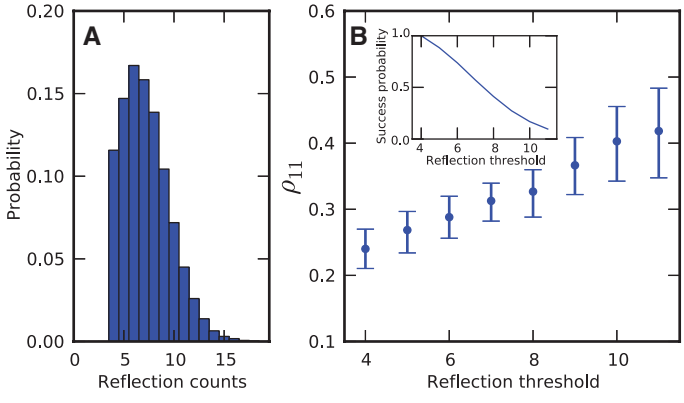

Fig. 3. Fidelity control of a W state with 41 atoms. (**A**) Distribution of counts in reflection during successful state preparation. The count rate in transmission is always zero, otherwise the preparation step is repeated. (**B**) Fidelity of the prepared W state and success probability as functions of the reflection threshold $N_{R,min}$. The data shown in Fig. 2B corresponds to $N_{R,min} = 11$, for which the preparation success is 9%. Error bars indicate 1 SD.

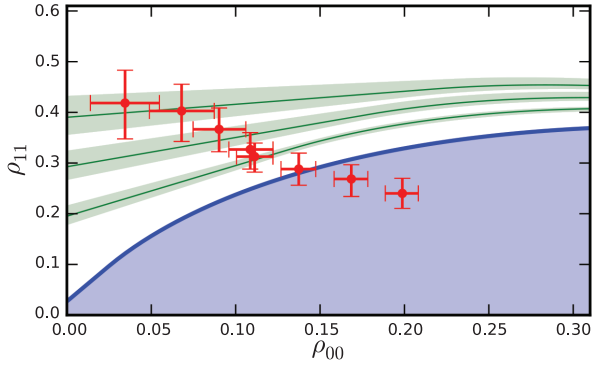

Fig. 4. Multipartite entanglement for a W state with 41 atoms. Fully separable states lie within the blue shaded area. From bottom to top, the green curves show the bound for k-separable states with k = 8, 12, and 16. A state above a bound contains at least $k + 1$ entangled particles. Shaded areas limit the bounds when varying the atom number from 37 to 45. The red points are the data from Fig. 3B, showing the increase of the minimal number of entangled particles with increasing $N_{R,min}$. Error bars indicate 1 SD.

Starting from this expression, we first calculate the upper bound for ρ_{11} as a function of ρ_{00} for a fully separable state with $k = 1$ (*21*). The bound, which is tight, is shown as the solid thick blue line in Fig. 4. Any state corresponding to a point outside the blue shaded region necessarily contains at least two-particle entanglement. The calculation can be extended to larger k, and the green lines show the bounds for $k = 8$, 12, and 16. The experimental state with the highest fidelity of 0.42 lies ~1 SD above the $k = 12$ curve, indicating that it contains at least 13 entangled atoms.

In our present setup, fidelity is limited by decoherence due to differential light shifts in the dipole trap (*21*) and a probability of ~0.2 for spontaneous emission from $|1\rangle$ during the QND detection. For large atom numbers, spontaneous emission from $|0\rangle$ will eventually become dominant. Simulations show that, with state-of-the-art optical cavities, the entanglement process can be scaled up to ensembles with $N > 10^4$. Because our method relies only on coherent evolution and collective QND measurement, it can be adapted to many systems and, in particular, to other forms of cavity quantum electrodynamics, including addressable qubits such as ions in optical cavities (*31*) or superconducting qubits in microwave cavities (*32*), as long as they are indistinguishable by cavity measurement. Furthermore, by including multiple rotations and QND detection intervals, or by combining it with other entanglement schemes such as cavity-induced spin squeezing (*6*), our scheme can be extended to a large range of entangled states. In combination with the inherent single-particle resolution, this makes it possible to investigate the fundamental limits of metrologically relevant forms of entanglement and could considerably enhance the precision of interferometric devices based on quantum metrology. In addition, our method is well suited to investigate quantum Zeno dynamics (*33*), where permanent QND observation of a degenerate eigenvalue limits the coherent evolution of the system to a given subspace, enabling preparation of a large variety of entangled states (*34*).

References and Notes

1. T. Monz *et al.*, *Phys. Rev. Lett.* **106**, 130506 (2011).
2. C. Gross, T. Zibold, E. Nicklas, J. Estève, M. K. Oberthaler, *Nature* **464**, 1165–1169 (2010).
3. M. F. Riedel *et al.*, *Nature* **464**, 1170–1173 (2010).
4. B. Lücke *et al.*, *Science* **334**, 773–776 (2011).
5. J. Appel *et al.*, *Proc. Natl. Acad. Sci. U.S.A.* **106**, 10960–10965 (2009).
6. M. H. Schleier-Smith, I. D. Leroux, V. Vuletić, *Phys. Rev. Lett.* **104**, 073604 (2010).
7. J. G. Bohnet *et al.*, Reduced back-action for phase sensitivity 10 times beyond the standard quantum limit. http://arxiv.org/abs/1310.3177 (2013).
8. M. Koschorreck, M. Napolitano, B. Dubost, M. W. Mitchell, *Phys. Rev. Lett.* **104**, 093602 (2010).
9. I. D. Leroux, M. H. Schleier-Smith, V. Vuletić, *Phys. Rev. Lett.* **104**, 073602 (2010).
10. S. Massar, E. S. Polzik, *Phys. Rev. Lett.* **91**, 060401 (2003).
11. A. Kuzmich, N. P. Bigelow, L. Mandel, *Europhys. Lett.* **42**, 481–486 (1998).
12. V. Giovannetti, S. Lloyd, L. Maccone, *Science* **306**, 1330–1336 (2004).
13. V. Vedral, *Nature* **453**, 1004–1007 (2008).
14. H. J. Kimble, *Phys. Scr.* **T76**, 127 (1998).
15. Y. Colombe *et al.*, *Nature* **450**, 272–276 (2007).
16. F. Brennecke *et al.*, *Nature* **450**, 268–271 (2007).
17. T. P. Purdy *et al.*, *Phys. Rev. Lett.* **105**, 133602 (2010).
18. S. Brakhane *et al.*, *Phys. Rev. Lett.* **109**, 173601 (2012).
19. J. Volz, R. Gehr, G. Dubois, J. Estève, J. Reichel, *Nature* **475**, 210–213 (2011).
20. A. D. Boozer, A. Boca, R. Miller, T. E. Northup, H. J. Kimble, *Phys. Rev. Lett.* **97**, 083602 (2006).
21. Materials and methods are available as supplementary materials on *Science* Online.
22. W. Dür, G. Vidal, J. I. Cirac, *Phys. Rev. A* **62**, 062314 (2000).
23. L. Pezzé, A. Smerzi, *Phys. Rev. Lett.* **102**, 100401 (2009).
24. C. W. Chou *et al.*, *Nature* **438**, 828–832 (2005).
25. T. Chanelière *et al.*, *Nature* **438**, 833–836 (2005).
26. F. T. Arecchi, E. Courtens, R. Gilmore, H. Thomas, *Phys. Rev. A* **6**, 2211–2237 (1972).
27. R. Gehr *et al.*, *Phys. Rev. Lett.* **104**, 203602 (2010).
28. S. L. Christensen *et al.*, Quantum interference of a single spin excitation with a macroscopic atomic ensemble. http://arxiv.org/abs/1309.2514 (2013).
29. J. M. Raimond *et al.*, *J. Phys. B* **38**, S535–S550 (2005).
30. O. Gühne, G. Tóth, *Phys. Rep.* **474**, 1–75 (2009).
31. B. Casabone *et al.*, *Phys. Rev. Lett.* **111**, 100505 (2013).
32. J. A. Mlynek *et al.*, *Phys. Rev. A* **86**, 053838 (2012).
33. P. Facchi, S. Pascazio, *Phys. Rev. Lett.* **89**, 080401 (2002).
34. J. M. Raimond *et al.*, *Phys. Rev. Lett.* **105**, 213601 (2010).

Acknowledgments: We thank G. Semerjian for help with the calculations on the entanglement criterion and B. Huard for discussions. This work was supported by the European Union Information and Communication Technologies project QIBEC (Quantum Interferometry with Bose-Einstein Condensates) (GA 284584) and the Integrating Project AQUTE (Atomic Quantum Technologies) (GA 247687). F.H. acknowledges a scholarship by Institut Francilien de Recherche sur les Atomes Froids. Author contributions: F.H. and J.V. performed the experiment; R.G. made contributions in its early stages; and F.H., J.V., J.R., and J.E. contributed to data analysis and interpretation, as well as to the manuscript.

Supplementary Materials

www.sciencemag.org/content/344/6180/180/suppl/DC1
Materials and Methods
Figs. S1 to S6
References (*35–37*)

25 November 2013; accepted 12 March 2014
Published online 27 March 2014;
10.1126/science.1248905

Unfolding the Laws of Star Formation: The Density Distribution of Molecular Clouds

Jouni Kainulainen,[1]* Christoph Federrath,[2] Thomas Henning[1]

The formation of stars shapes the structure and evolution of entire galaxies. The rate and efficiency of this process are affected substantially by the density structure of the individual molecular clouds in which stars form. The most fundamental measure of this structure is the probability density function of volume densities (ρ-PDF), which determines the star formation rates predicted with analytical models. This function has remained unconstrained by observations. We have developed an approach to quantify ρ-PDFs and establish their relation to star formation. The ρ-PDFs instigate a density threshold of star formation and allow us to quantify the star formation efficiency above it. The ρ-PDFs provide new constraints for star formation theories and correctly predict several key properties of the star-forming interstellar medium.

The formation of stars is an indivisible component of our current picture of galaxy evolution. It also represents the first step in defining where new planetary systems can form. The physics of how the interstellar medium (ISM) is converted into stars is strongly affected by the density structure of individual molecular clouds (*1*). This structure directly affects the star-formation rates (*SFRs*) and efficiencies (*SFEs*) predicted by analytic models (*2–5*). Inferring this structure observationally is challenging because observations only probe projected column densities. Hence, the key parameters of star-formation models remain unconstrained. Here, we present a technique that allows us to quantify the grounding measure of the molecular cloud density structure: the probability density function of their volume density (ρ-PDF).

The *SFRs* of molecular clouds are estimated in analytic theories from the amount of gas in the clouds above a critical density, ρ_{crit} (*2–5*)

$$SFR = \frac{\varepsilon_{core}}{\phi} \int_{s_{crit}}^{\infty} \frac{t_{ff}(\rho_0)}{t_{ff}(\rho)} \frac{\rho}{\rho_0} \, p(s)\mathrm{d}s \qquad (1)$$

where $s = \ln(\rho/\rho_0)$ is the logarithmic, mean-normalized density, and $s_{crit} = \ln(\rho_{crit}/\rho_0)$. We use the number density, $n = \rho/\bar{\mu}m_p$, where $\bar{\mu}$ is the mean molecular mass and m_p is the proton mass, as the measure of density. The parameter ε_{core} in Eq. 1 is the core-to-star efficiency, giving the fraction of gas above s_{crit} that collapses into a star. The $t_{ff}(\rho)$ is the free-fall time of pressureless gas that approximates the star-formation time scale, and ϕ is the ratio of the free-fall time to the actual star-formation time scale. The critical density, commonly referred to as the (volume) density threshold of star formation, indicates that stars form only above that density. Generally, the critical density depends on gas properties (*2–5*), but theoretical considerations suggest that it could be relatively constant under typical molecular cloud conditions (*5*).

[1]Max-Planck-Institute for Astronomy, Königstuhl 17, 69117 Heidelberg, Germany. [2]Monash Centre for Astrophysics, School of Mathematical Sciences, Monash University, Vic 3800, Australia.
*Corresponding author. E-mail: jtkainul@mpia.de

Entangled States of More Than 40 Atoms in an Optical Fiber Cavity

Florian Haas, Jürgen Volz, Roger Gehr, Jakob Reichel and Jérôme Estève (March 27, 2014)

Science **344** (6180), 180-183. [doi: 10.1126/science.1248905] originally published online March 27, 2014

Editor's Summary

All Together Now

In quantum entanglement, correlations between particles mean that the measurement of one determines the outcome of the other(s). Generally, when trying to exploit quantum entanglement, the larger the number of entangled particles, the better. However, the size of entangled systems has been limited. **Haas *et al.*** (p. 180, published online 27 March; see the Perspective by **Widera**) prepared a small ensemble of ultracold atoms into a collective entangled state. Starting from one internal quantum state, the system of cold atoms was excited with a weak microwave pulse leading to a small excitation probability. Because it is not known which atom is promoted into the excited state, the detection of one quantum of excitation projects the system into an entangled quantum state, called a W-state. A fast repeat-until-success scheme produced such W-states quasi-deterministically. Using such a technique was able to yield entangled states of more than 40 particles. The relatively large ensemble-entangled states could potentially in the future find use in quantum sensing or enhanced quantum metrology applications.

Science (print ISSN 0036-8075; online ISSN 1095-9203) is published weekly, except the last week in December, by the American Association for the Advancement of Science, 1200 New York Avenue NW, Washington, DC 20005.